Accepted Manuscript

Microstructure of selective laser melted CM247LC nickel-based superalloy and its evolution through heat treatment

V.D. Divya, R. Muñoz-Moreno, O.M.D.M. Messé, J.S. Barnard, S. Baker, T. Illston, H.J. Stone

Please cite this article as: Divya VD, Muñoz-Moreno R, Messé OMDM, Barnard JS, Baker S, Illston T, Stone HJ, Microstructure of selective laser melted CM247LC nickel-based superalloy and its evolution through heat treatment, *Materials Characterization* (2016), doi: 10.1016/j.matchar.2016.02.004

Microstructure of selective laser melted CM247LC nickel-based superalloy and its evolution through heat treatment

V.D. Divya[1], R. Muñoz-Moreno[1], O.M.D.M Messé[1], J.S. Barnard[1], S. Baker[2], T. Illston[2], H.J. Stone[1]

[1]Department of Materials Science and Metallurgy, University of Cambridge, 27 Charles Babbage Road, Cambridge CB3 0FS, UK

[2]Materials Solutions, Unit 8, Great Western Business Park, McKenzie Way, Worcester, WR4 9GN, UK

Abstract

The selective laser melting of high temperature alloys is of great interest to the aerospace industry as it offers the prospect of producing more complex geometries than can be achieved with other manufacturing methods. In this study, the microstructure of the nickel-based superalloy, CM247LC, has been characterised following selective laser melting and after a post deposition heat-treatment below the γ' solvus temperature. In the as-deposited state, scanning electron microscopy with electron backscatter diffraction revealed a fine, cellular microstructure with preferential alignment of <100> along the build direction. A high dislocation density was seen at the periphery of the cells, indicating substantial localised deformation of the material. Fine primary MC carbides were also observed in the inter-cellular regions. High-resolution transmission electron microscopy identified the occurrence of very fine γ' precipitates, approximately 5 nm in diameter, dispersed within the gamma phase. After heat treatment, the elongated cell colonies were observed to partially coalesce, accompanied by a decrease in dislocation density, producing columnar grains along the build direction. Cuboidal γ' precipitates approximately 500 nm in diameter were observed to form in the recrystallised grains, accompanied by larger γ' precipitates on the grain boundaries.

1. Introduction

Over the last few years, additive manufacturing (AM) techniques have received considerable attention due to their ability to produce components with complex geometries that cannot be fabricated by other techniques [1,2]. This potentially allows components to be produced with fundamentally new architectures and, therefore, the prospect of new, more efficient component designs. For specific applications, AM also offers the prospect of minimising material loss, hence reducing finished component cost. Amongst AM techniques, selective laser melting (SLM) utilises the selective densification of a pre-alloyed powder by melting a powder bed in a layer-by-layer manner through scanning or rastering a laser beam in a path that defines the geometry desired [2-4].

In the power generation and aerospace industries, the high temperatures and stresses that must be tolerated by certain components in gas turbine engines necessitate the use of nickel-based superalloys. As such, the amenability of this class of alloys to processing by AM techniques, including SLM, has received much interest [5-7]. With such techniques, epitaxial growth of columnar grains occurs along the build direction resulting in microstructures that have been compared to those of directionally solidified superalloys [7-10]. Studies of nickel-based superalloys processed through AM techniques have shown that the deposition parameters such as laser power, laser scan strategy and laser scan speed have a strong effect on the solidification structure of the deposits. Parimi *et al.* [11] have shown that a high laser power results in a columnar grain structure with a strong <001> texture along the build direction. Dinda *et al.* [12] reported that a unidirectional scan pattern gave rise to a fiber texture, while a backward and forward scanning pattern lead to a rotated cube texture. Carter *et al.* [13], in their island scan strategy, found columnar grains with a strong texture in the island centres, while the boundaries showed finer elongated grains, with no discernible texture. Recently, Wei *et al.* [14] reported a numerical model of the solidification growth patterns produced by AM to tailor the texture and to improve the resultant mechanical properties.

In addition to affecting the solidification textures, the processing parameters have a strong effect on the other microstructural features. With lower power densities during deposition, very rapid cooling rates are achieved which lead to refined microstructural features. As a

result, AM processed alloys have been seen to exhibit improved properties compared to their conventionally processed counterparts. From the TEM observations on the as-SLM state of IN939, Kanagarajah *et al.* [15] reported elongated microstructures composed of low-angle boundaries in the build direction, which possessed superior tensile properties than the cast condition. However, the resultant microstructures may not always be favorable. For example, Kunze *et al.* [16] reported that the strong crystallographic textures in IN738LC processed by SLM, lead to pronounced anisotropy in the mechanical properties.

SLM processing has also been shown to strongly influence γ' precipitation behavior. In the SLM processed IN939 [15], the γ' phase was detected only after ageing heat treatment. In a study by Zhang *et al.* [17] the microstructure of IN718 in the as-deposited state was shown to comprise of fine cells with limited precipitation of γ' and γ'', as well as a high density of dislocations at the cell boundaries. Due to very high cooling rate encountered during the solidification of SLM processed materials, post-SLM heat treatments are necessary to develop γ' precipitates to the desired size. For example, HIPing of the SLM processed IN718 at 1163°C, has been reported to give uniformly distributed 250 nm sized γ'' precipitates within the recrystallised regions [18]. Additionally, heat treatment may also be necessary to relieve the residual stresses generated as a result of differential thermal contraction of successive layers during deposition. Heat treatments may also be used to reduce the anisotropy in the deposited samples by allowing recrystallisation. However, the conditions required to achieve this have been shown to vary from alloy to alloy. In a study by Etter *et al.* [19], it was shown that substantial recrystallisation takes place in Hastelloy X following heat treatment for 4 hours at 1200°C. In contrast, Kunze *et al.* [16], observed no recrystallisation or grain growth in SLM-processed IN738LC after several hours at 1180°C.

To date, studies of nickel-based superalloys processed by AM techniques have provided insight into the influence of the deposition parameters and the alloy chemistry on the final microstructure. However, there remains a lack of detailed understanding of the nucleation and growth of γ' precipitates, during SLM processing and through subsequent heat treatments. This is particularly important for those nickel-based superalloys that have high γ' volume

fractions needed for high temperature service as such superalloys are more prone to processing issues and defects during AM. In the present study, the microstructure of the high γ′ volume fraction alloy CM247LC in the as-SLM state has been characterised in detail using scanning electron microscopy, as well as conventional and high-resolution transmission electron microscopy. Electron back-scattered diffraction was also performed across a range of length scales to characterise the texture variations across the material. In addition, the microstructural changes that take place after heat treatment below the γ′ solvus temperature have been determined and related to the as-SLM microstructure. A comparison of these microstructures to conventionally-cast CM247LC has also been made.

2. Material and experimental method

CM247LC was supplied by LPW Technology Ltd., UK, as a pre-alloyed, gas-atomised powder with a log-normal particle size distribution varying between 15 and 70 μm. The composition of the alloy provided by the supplier is given in **Table 1.** As shown in **Fig. 1**, the powder particles were mostly spherical, although satellites and morphological irregularities were also observed. Selective laser melting was carried out under an argon atmosphere (oxygen level < 0.1%) using a 200 W IPG ytterbium fibre laser onto a base plate of DIN 1.1730 grade tool steel, maintained at 80˚C. A succession of 20 μm thick layers of CM247LC powder was spread over the base-plate and consolidated by rastering a laser beam. A schematic representation of the laser deposition strategy used to produce a cylindrical specimen is presented in **Fig**. **2**. The reference frame used to describe the build process is shown in **Fig. 2a**, overlaid on a block of three deposited layers. The laser scan pattern was rotated by an angle of 67˚ between successive layers along the Z-direction, following the approach of Dimter *et al.* [20] in order to homogenise the heat flow during the consolidation process, as well as to reduce both manufacturing defects and to relieve stresses, **Fig. 2b**. Within the XY plane of each layer, the area was divided into stripes **(Fig. 2c)** by melting the powder on the stripe primarily. Between these stripes, the laser beam was continuously scanned in a back and forth manner, as represented in the region marked by the white circle in **Fig. 2c**. As indicated by the enlarged view in **Fig. 2d**, there was an overlap between each laser scan during consolidation. After completion of the laser

deposition process, the specimen was detached from the base-plate via electro discharge machining (EDM) and sectioned for examination using the techniques described below.

To ascertain the effect of high temperature heat treatment on the microstructure, a 10 mm thick slice of the as-SLM sample was encapsulated in an argon back-filled quartz ampoule. The encapsulated sample was then subjected to heat treatment at 1230°C for 2 hours, followed by air-cooling. Samples in this microstructural condition are subsequently referred to as SLM+HT.

CM247LC in the conventionally cast (CC) state was supplied by Rolls-Royce plc. Derby, UK and subjected to a solution heat-treatment of 1260°C for 18 hours followed by air-cooling. The sample was further aged at 870°C for 18 hours before furnace cooling. Sections of the heat-treated sample were prepared using the same protocols as the as-SLM and SLM+HT samples, to allow comparison between the resultant microstructures.

Phase transformation temperatures were determined using differential scanning calorimetry (DSC) with a NETZSCH 404 calorimeter. Circular discs, 5 mm in diameter and with an average thickness of 1.3 mm, were used for the thermal analysis. The measurements were carried out in an argon atmosphere, with a flow rate of 50 mL min^{-1}. The heat flux was recorded as the samples were heated at a rate of 10°C min^{-1} from room temperature to 1450°C before cooling back to room temperature at the same rate. The data acquired during the heating cycle was used to determine the phase transformation temperatures.

The phases present were characterised using a Bruker D8 X-ray diffractometer, with CuK$_\alpha$ radiation operated at 40 kV and 40 mA. A nickel filter, 0.012 mm thick, was used to suppress K$_\beta$ peaks in the XRD profile. Each scan was performed across the angular range (2θ) from 20° to 80°, with a step size of 0.05° and a dwell time of 5 s.

Representative transverse and longitudinal sections of the SLM specimens, perpendicular and parallel to the build direction (Z) respectively, were prepared for microstructural analysis. The specimens were mounted in a conductive Bakelite resin, ground with a succession of SiC papers before being polished to a mirror finish using 0.04 μm colloidal silica suspension. In addition, in order to characterise the γ′ precipitates, samples were etched in Kalling's reagent (5 g CuCl$_2$ + 100 mL HCl + 100 ml distilled water).

The microstructures of the samples were imaged using scanning electron microscopy (SEM) in a CamScan-MX2600 field emission gun (FEG) microscope, equipped with an Oxford Instruments INCA energy dispersive X-ray spectroscopy (EDX) detector and Channel 5-HKL electron back- scatter diffraction (EBSD) system, as well as in a Nova NanoSEM 450. The microscopes were operated at 20 kV and ESBD scans were performed with a step size of 0.3 μm, unless specified otherwise. The EBSD orientation maps were always plotted with respect to the build direction (i.e. the Z-axis). Subsequent analysis of the Euler angles obtained from the Channel 5-HKL software was performed using MATLAB, combined with the MTex software (version 4.0.9) [21].

The microstructure of the as-SLM and SLM+HT samples were examined using transmission electron microscopy (TEM). For these studies, 3 mm diameter discs with a thickness of 200 μm were prepared, before being thinned using a Struers twinjet Tecnupol-5 electropolisher operated at 13 V. The electropolishing solution consisted of 10 vol. % perchloric acid in methanol, maintained at -5°C ± 1°C. TEM investigations were carried out in JEOL-200CX and FEI Tecnai Osiris microscopes operated at 200 kV, with the latter equipped with an FEI Super-X EDX detector. The FEI Tecnai Osiris was operated in both conventional TEM and scanning TEM (STEM) modes.

The Vickers hardness of the alloy in the three different microstructural states (as-SLM, SLM+HT & CC) was measured using a 200HV-5 micro-hardness rig, with a 5 kN load. For each sample, 15 measurements were performed from which an average value was taken.

The equilibrium phase fractions and phase transformation temperatures of CM247LC were predicted with the thermodynamic modeling software, Thermocalc, using both the TCNI5 [22] and TTNI8 [23] databases. In these calculations, only the liquid, γ, γ' and MC carbide phases were considered.

SEM images were captured in the back-scattered electron (BSE) mode to accentuate the pores and cracks. These images were subsequently analysed using the image processing software, ImageJ [24], to quantify the area fraction of porosity and the length of cracks present in the as-SLM state.

3. Results

3.1 Thermal analysis

The DSC thermograms acquired during heating samples of CM247LC in the three different microstructural states are presented in **Fig. 3**. The data obtained on cooling are not shown, as only the data obtained during the initial heating cycle are representative of the thermo-mechanical history of the samples prior to testing. In all three microstructural states, an abrupt change in heat flow was observed at around 1250°C, associated with the start of dissolution of γ' precipitates. For the as-SLM sample, this change initiated at 1254°C, whilst that of the SLM+HT sample began at 1246°C. In both of these samples, dissolution of γ' precipitates was seen to be complete by 1265°C, and this was taken to be the solvus temperature of the γ' phase, $T_{\gamma'}$. In contrast, the alloy in the CC state showed complete dissolution of the γ' phase at the lower temperature of 1252°C. As the onsets of melting for the three microstructural conditions were not sharply defined in the DSC thermograms, the solidus temperature, T_s, for each sample was determined from the associated DSC thermogram using the deflection from baseline method reported by Boettinger *et. al* [25]. In the as-SLM and SLM+HT samples, the solidus temperature was observed to occur at 1279°C, whilst in the CC state the solidus occurred at the higher temperature of 1295°C. However, it was noted that the proximity of the γ' solvus and the onset of melting made unambiguous determination of the solidus temperature difficult. In all three microstructural states, a noticeable change in heat flow was detected within 1°C of 1356°C and this was attributed to the start of dissolution of the carbides, T_c. The liquidus temperature, T_L, of all of the samples was observed to occur at 1373°C. The key transformation temperatures determined by DSC are summarised in **Table 2**.

3.2 Thermodynamic equilibria calculations

The equilibrium phase fractions predicted using Thermocalc with the TCNI5 and TTNI8 databases as a function of temperature are presented in **Fig. 4** and the key transformation temperatures obtained from these results are summarised in **Table 2**. The liquidus, solidus and carbide dissolution temperatures predicted using TTNI8 were all in good agreement with the experimental values, noting that the solidus could not be reliably

determined from the as-SLM and SLM+HT samples. In contrast, the agreement between the experimental transition temperatures and those predicted using TCNI5 was poor, with the liquidus temperature being over predicted and both the solidus and carbide dissolution temperatures being under predicted.

In spite of the poor correlation between the experimentally determined liquidus, solidus and carbide dissolution temperatures with those predicted using TCNI5, the γ' solvus temperature obtained with this database was in better agreement with the measured values than that predicted using TTNI8.

3.3 Characterisation of the as-SLM microstructure

BSE micrographs of the as-SLM sample parallel and perpendicular to the build direction are presented in **Fig. 5a** and **b** respectively. Inverse pole figure maps with respect to the build direction (IPF-Z) obtained from the EBSD scans performed on the same regions are shown in **Fig. 5c** and **d**. From these images, it can be seen that the microstructure was composed of elongated columnar grains along the build direction, crossing multiple deposited layers, **Fig. 5a** and **c**. The grain size varied noticeably along each direction. Along the build direction (Z-axis), the Feret length of the grains varied from 100 to 200 μm, whilst the Feret length perpendicular to the Z-axis was much smaller, being in the range 10 to 40 μm.

In the transverse direction, **Fig. 5b** and **d**, a bimodal distribution of grains was observed: (i) elongated grains with a Feret diameter of 40 to 50 μm along their length and 10 to 20 μm across; (ii) clusters of small equiaxed grains approximately 5 μm in diameter. The morphologies and spatial distributions of the grains were consistent with the laser scan path, as they followed a band pattern with dimensions similar to those presented in **Fig. 2d**. The smaller grains were usually surrounded by bands of elongated grains, with a width similar to the diameter of the laser beam. Such bands are highlighted by white lines in **Fig. 5b.** As each traverse partially overlapped the previous one, some remelting occurred, leading to the formation of the small grains. Limited occurrences of small grain clusters were also observed in the longitudinal cross section, **Fig. 5c**.

The bands of elongated grains were consistent with lateral growth of grains from the fusion boundary during solidification, parallel to the direction of the greatest thermal gradient. However, as each deposited layer was only 20 μm thick, very precise sectioning would be required in order to capture an entire band within the observation plane. The elongated grains bounding the banded regions in **Fig. 5b** and **d** were associated with partial sectioning through the layers above and below the principal layer examined. These layers were both rotated 67˚ from each other.

The EBSD maps obtained from the longitudinal and transverse sections, **Fig. 5c** and **d**, clearly show the presence of a strong texture with <001> aligned along the build direction. It can also be observed from the BSE micrograph and the associated IPF-Z from the longitudinal section, **Fig. 5a** and **c,** that columnar grains sharing a common orientation extend across multiple deposited layers. In both IPF-Z maps, significant misorientations within the grains can be observed. These misorientations have been highlighted by plotting the corresponding intragranular misorientation (IGM) maps, **Fig. 5e** and **f**. These figures confirm the presence of misorientations within grains that are typically less than 4˚, although more isolated regions of higher misorientations were also observed.

Pole figures of the {001} planes obtained from the EBSD data from the longitudinal and transverse sections are given in **Fig. 6a** and **b** alongside the associated normalised misorientation distributions weighted by the grain area, **Fig. 6c** and **d**. The occurrence of high intensity in the centre of the pole figures is consistent with the presence of a strong cube texture in the build direction. However, there is no evidence of preferential alignment in the XY plane. In addition, the inferior statistics associated with the longitudinal section data was attributed to the sampling of fewer grains in this orientation over the same area and limited the confidence with which conclusions could be drawn from these data. The misorientation histograms show log normal distributions with peak frequencies of 0.90 and 0.81 in the longitudinal and transverse sections. In both distributions, 95% of misorientations occur with angles of less than ~ 4˚. The maximum misorientations recorded in the longitudinal and transverse sections were 11˚ and 16˚ respectively.

Examination of the as-SLM sample at higher magnification revealed the presence of a

fine cellular structure within each grain, **Fig. 7a**. These cells appeared equiaxed in the section examined and can be visualised as rods, with a diameter of about 500 nm extending along the length of the grain. A similar structure was reported by Carter *et al.* [13], although in that study, the cells were mistaken for fine elongated grains. In **Fig. 7a,** fine particles were also observed on the cell boundaries. The bright contrast of these particles in BSE imaging was indicative of elevated concentrations of elements with high atomic number. This was confirmed through TEM-EDX mapping, the results of which are discussed in a later section. Less abundant, larger particles were also observed, of a size amenable to SEM-EDX characterisation. The largest particles were spherical and found to be (Hf, Al) rich oxides. It is conceivable that these oxides originated from impurities and moisture present on the powder particle surfaces. It is also possible that interaction with the environment during the deposition process may have contributed to oxide formation. The smallest particles were identified as being Hf-rich MC carbides and arise a result of the high carbon and refractory metal content of the alloy.

To evaluate further the orientation distribution of the cells in the grains, an EBSD map was collected with a finer step size of 0.05 μm. A single grain within the field of view was identified by setting a threshold on the inter-pixel misorientation angle of 1˚. The average orientation of all data points within this grain was determined and an orientation map was generated centred on the mean grain orientation. This orientation map is given in **Fig. 7b** and the associated mean grain orientation is identified by the red cross in the IPF-Z given in the figure legend. The blue points on the IPF-Z show the orientations of the individual data points. This method enabled small areas of uniform colour to be associated with individual cells in **Fig. 7a**. The uniformity of colour within a cell suggests that it has a single orientation, but those small misorientations between adjacent cells leads to gradual variations across the colonies. These observations are consistent with the progressive change in misorientation across grains identified in **Fig. 5c** to **f**.

In order to provide more detailed information about the microstructure, TEM analysis was performed. A bright field image of a region containing several cells, viewed parallel to the cell axes is given in **Fig. 8a**. As with the EBSD analysis, the cells exhibited different

10

orientations, which is clearly evidenced by the difference in contrast in **Fig. 8a**. This is further supported by the [110] selected area diffraction pattern obtained from this area, **Fig. 8b**, which shows spot asymmetry and multiple spots for each reflection, associated with small crystal misorientations. From this diffraction pattern, the maximum misorientation about the [110] axis for the area selected was determined to be 7˚. This value is in line with the data obtained from the EBSD analysis, presented in **Fig. 7**. Carbides, approximately 50 nm in size, could also be identified at the cells walls. A bright field image of another area of the TEM specimen showing elongated cells is given in **Fig. 8c**. Both **Fig. 8a** and **Fig. 8c** show extensive networks of dislocations on the cell boundaries. Dislocations were also observed within the cells, but at a much lower density. These dislocations were very tortuous, and appeared to be dissociated into partials. Closer examination of the dislocations in the cells in **Fig. 8a** and **c** revealed the presence of serrations along their lengths, suggesting the interaction with smaller, unresolved intra-cellular particles. Faint superlattice reflections were also observed in the selected area diffraction pattern in **Fig. 8b**. These observations were consistent with the presence of γ′ precipitates in the microstructure. To directly characterise these particles, dark field imaging from a superlattice reflection was performed, **Fig.9a**. This image showed the presence of a bimodal distribution of γ′ precipitates, with very fine intracellular precipitates, along with larger precipitates about 50 nm in size, located at the cells boundaries. The intracellular precipitates were identified from their Moiré fringes using higher resolution imaging, **Fig.9b** and found to be about 5 nm in size.

To investigate the extent of elemental microsegregation at the cellular scale and determine the composition of the carbides, maps of elemental concentration were constructed from STEM- EDX data obtained close to the <001> axis over an area encompassing several cells, **Fig.10**. The first subfigure shows a HAADF image of the region of interest, in which two cells, labeled 'a' and 'b' are highlighted. The subsequent subfigures show qualitative concentrations of each of the elements listed, along with the electron transition from which they were determined. The difference in the intensity of the colours of cells 'a' and 'b' is attributed to the local orientation of the cells; in cells on the zone axis, the beam interaction is smaller, hence generating a weaker signal, than those more off-axis. The elemental concentration maps show that the boundaries are slightly enriched with the Al, Ti, and Cr,

whilst the particles visible at the cell boundaries were found to be rich in Ti, Hf, Ta, Mo and W. This enrichment is consistent with these particles being MC carbides. Interestingly, Al was also found to segregate to these carbides, which suggests that these are metastable carbides. The γ' precipitates could not be characterised directly using STEM-EDX at this magnification due to their fine size. However, enrichment of Al and Ti at the cell boundaries may have promoted their formation in these regions, leading to the larger γ' precipitates observed.

3.4 Characterisation of the SLM+HT microstructure

BSE micrographs of the SLM+HT sample from the longitudinal and transverse sections are given in **Fig.11a** and **b** respectively. EBSD data from the same regions are presented as IPF- Z maps in **Fig.11c** and **d**. The microstructures seen in both sections were similar to those observed in the as-SLM condition, with elongated, columnar grains along the build direction that cross multiple deposited layers. However, the EBSD IPF-Z maps indicate that the heat-treatment reduced the texture compared to the as-SLM condition and caused limited, localised recrystallisation. This is most apparent with the large green grain on the left hand side of **Fig.11c**. In the associated IGM map, **Fig.11e**, this grain exhibits little to no internal misorientation, having a uniform dark blue colour. Similar features may be identified in the transverse section EBSD IPF-Z map, **Fig.11d** and corresponding IGM map, **Fig.11f**. For example, the large pink and blue grains located towards the centre of **Fig.11d**. The observation of recrystallisation is consistent with significant energy stored in the dislocation networks [26,27]. Although limited recrystallisation was observed following heat treatment at 1230˚C.

The {100} pole figures obtained from the EBSD IPF-Z maps of the longitudinal and transverse sections are presented in **Fig.12a** and **b**. As with the data acquired from the specimen in the as- SLM condition, the limited number of grains sampled in the longitudinal section resulted in inferior statistics compared to that obtained from the transverse section. In both sections, a strong cube texture was seen in the build direction, with limited evidence of preferential secondary orientation. However, the presence of large

recrystallised grains in the microstructure resulted in additional, localised intensity in the pole figures. The normalised misorientation distributions weighted by the grain area in both the longitudinal and transverse sections are shown in **Fig.12c** and **d**. This data reduction method avoids the data being biased towards the orientations of the large, recrystallised grains. As with the data obtained from the as-SLM condition, the misorientation histograms are well described by log-normal distributions. Whilst the widths of these distributions and maximum misorientations are broadly similar to those seen in **Fig.12c** and **d**, the peak frequencies are lower, being 0.75 and 0.68 in the longitudinal and transverse sections respectively, and have shifted towards lower misorientation angles. These changes are consistent with the presence of the large recrystallised grains, which show little to no internal variation in misorientation. Higher resolution BSE imaging of an etched sample of the alloy in the SLM+HT condition is shown in **Fig.13a**. The microstructure contains three distinct morphologies of γ' precipitates: (i) irregularly shaped γ' precipitates, 1-2 µm in size, predominantly located at the boundaries of the recrystallised grains and cell colonies; (ii) smaller cuboidal precipitates, 200-500 nm in size, uniformly distributed within the recrystallised grains; (iii) small precipitates of a similar size but more irregular morphology, uniformly distributed within the unrecrystallised grains. The morphology of the intra-granular γ' precipitates in the recrystallised grains was similar to that previously reported for conventionally cast CM247LC [28]. In addition, carbide particles were identified, ranging from 200 to 500 nm in size. Whilst these carbides were predominantly located at the grain boundaries in chain-like configurations, some were also found inside the grains.

Transmission electron microscopy of the recrystallised and non-recrystallised regions revealed subtle differences in the shape and distribution of the γ' precipitates in these regions. A bright field image of an unrecrystallised region is shown in **Fig.13b**. In this figure, two γ' precipitates are identified that have formed at the prior cellular boundaries and which show irregular morphologies. The occurrence of γ' precipitates at the cellular boundaries is consistent with more rapid diffusional transport of solute in these regions, facilitated by the high initial dislocation densities in the as-SLM condition. The density of dislocations in the SLM+HT sample, **Fig.13b**, is significantly lower than that observed in the as-SLM state, **Fig. 8a**. In addition, cells that have similar orientations and therefore comparable contrast in this imaging condition, such as those at the lower left hand side of the micrograph, exhibit

intercellular boundaries that appear to be free from dislocations. Conversely, the boundaries between cells that have more significant differences in crystallographic orientation contain visible, though reduced, dislocation networks and unpinned dislocations, as identified by the arrows in **Fig.13b**. These observations are consistent with dislocation recovery having occurred in these regions during the heat treatment. This has led to the apparent merging of similarly orientated cells into grains, whilst the retention of inter-cellular misorientations between poorly aligned cells has preserved the spread in crystallographic orientations across grains, as shown by the histograms obtained from the associated EBSD data in **Fig.12c** & **d**.

A dark field image obtained from a γ' superlattice reflection of a region that had undergone recrystallisation during the heat treatment is shown in **Fig. 12c**. In this region a bimodal distribution of γ' precipitates was observed, comprising cuboidal secondary γ' precipitates approximately 200 to 400 nm in size, accompanied by finer tertiary γ' of the order of 50 nm. Isolated occurrences of fine carbides were also observed, as highlighted in the micrograph.

To examine the nature of the carbides observed in the microstructures of CM247LC, X-ray diffraction spectra were acquired from the samples in the as-SLM, SLM+HT and CC conditions, **Fig.14**. As expected, the diffraction spectra were dominated by the fundamental reflections from the γ and γ' phases. Importantly, the majority of the weaker reflections were consistent with the presence of MC carbides only. In the as-SLM condition, the MC carbide reflections were observed to occur at higher diffraction angles than those seen in the spectrum from the CC sample. This was attributed to compositional differences between the carbides formed during SLM processing, which may be metastable as a result of the rapid cooling, and those produced through casting and subsequent heat treatment, which may be closer to thermodynamic equilibrium. This hypothesis is supported by the results obtained from the SLM+HT sample, which showed two sets of MC carbide reflections; the stronger reflections were consistent with those observed in the CC sample and a weaker set were consistent with those seen in the as-SLM sample. This suggests that the post SLM heat treatment allowed redistribution of elements between the carbides that initially formed and their surrounding matrix, forming two distinct populations. The lattice parameters obtained from these reflections span the range reported for MC carbides

containing Hf, Ta and Ti [29,30]. However, more detailed characterisation would be required to unambiguously determine their respective compositions.

To evaluate the effect of the microstructural differences between CM247LC in the as-SLM, SLM+HT and CC conditions on the mechanical properties, hardness tests were performed. In the as-SLM condition, a hardness of 400 ± 9 HV was obtained. This was significantly lower than the value of 512 ± 9 HV obtained from the sample in the SLM+HT state. In contrast, the coarser, multi-modal γ' precipitate distributions in the SLM+HT microstructure provide significant strengthening. Although the as-SLM material contained a higher dislocation density than the SLM+HT state, the hardening afforded did not compensate for the reduced precipitate strengthening. The hardness of CM247LC in the CC state was measured to be 553 ± 34 HV. This value was higher than that obtained from the alloy in the SLM+HT condition and was attributed to a more optimal γ' precipitate size distribution. Interestingly, the greater standard deviation in hardness measured in the CC state suggested that SLM processing allows the development of a more homogeneous microstructure, even accounting for the variable extents of recovery and recrystallisation across the SLM+HT material.

3.5. Manufacturing defects

Cracks and porosity were observed in the as-SLM condition of CM247LC. A representative BSE micrograph of a large area from the transverse section near the periphery of the sample is shown in **Fig. 15a** and a higher magnification image in the vicinity of one of the cracks is given in **Fig. 15b**.

Pores with sizes varying from 0.5 to 20 µm were randomly distributed across the sample and constituted approximately 0.013 area % of the section examined. Two types of porosity were identified; small pores associated with gas bubbles that formed during the melting, and large pores generated by inclusions removed during the sample preparation. The origin of the larger pores from inclusions was elucidated through SEM-EDX analysis of the surrounding material, which exhibited higher concentrations of both Hf and Al than the

matrix (46 wt.% more Hf and 4 wt.% more Al).

The spatial distribution of the cracks was found to be inhomogeneous throughout the specimens. Cracking was observed to be more prevalent at the edge of the specimens than in the bulk and propagated over longer distances. The average crack length at the periphery of the sample was estimated to be 1.15 $mm.mm^{-2}$. Although, it was noted that cracks often formed discontinuous paths across the sample. In contrast, the average crack length in the centre of the sample was 0.3 $mm.mm^{-2}$ and occurred more commonly as isolated cracks.

Examination of a crack at higher magnification, **Fig. 15b**, revealed both inter- and intra-granular propagation modes, preferentially following cell boundaries. As a result, the crack paths were observed to be either straight or serrated, depending upon whether the section examined was parallel to or perpendicular to the principal axes of the columnar cells. In the longitudinal direction, some of the cracks were observed to cross multiple deposited layers, suggesting that cracking was not confined to the solidifying material alone during deposition. The density of cracks in the longitudinal section appeared to be lower than that of the transverse section, being 0.6 $mm.mm^{-2}$ at the specimen's periphery and 0.25 $mm.mm^{-2}$ at its core, although this may be a sectioning effect. Notably, due to the three dimensional character of the crack, it was difficult to pinpoint the precise location of crack initiation. Given the local misorientations between the cells and the high dislocation densities observed at their boundaries, **Fig. 8a**, significant deformations and stress concentrations must have been present, encouraging crack initiation and propagation in these regions.

4. Discussion

Low and high magnification BSE images of the microstructure of the conventionally cast CM247LC in the supersolvus heat-treated condition are shown in **Fig. 16a and b.** The microstructure comprised 100-150 µm grains containing a bimodal distribution of γ' precipitates. The secondary and tertiary γ' precipitates were 300 to 400 nm and ~50 nm, respectively. Having been subjected to a supersolvus heat treatment, no primary γ' precipitates were present at the grain boundaries. In addition, the CC microstructure contained a dispersion of MC carbides at the grain boundaries. In contrast, the microstructure of the as-

SLM CM247LC investigated in this study was markedly different. Layer-wise melting of the alloy led to epitaxial growth of columnar grains in which the crystallographic orientation is based on the bottom of the melting pool. This solidification mode generated material with a strong cube texture along the build direction. These columnar grains were formed of distinct cylindrical cells that had small misorientations with respect to one another. Very high temperature gradients generated during SLM processing subjected adjacent areas of the material to large strains as a result of differential thermal contraction. These strains induced localised plastic deformation and this was reflected by the appearance of high dislocation densities, primarily at the cell boundaries. The high temperature gradients also inhibited the growth of γ′ precipitates, which remained very small, being around 5 nm, and were homogeneously distributed throughout the cells (**Fig. 8**). However, larger γ′ precipitates were also identified at the cells boundaries, suggesting that the internal energy at these locations was sufficient for precipitates to form and grow. This energy may be provided by both the elevated dislocation densities and the local enrichment of Al and Ti from solidification-induced microsegregation in the vicinity of the cell boundaries. The kinetics of this process is further facilitated by the presence of the dislocations, which provide a lower energy diffusion path. With the exception of the microsegregation detected at the cells boundaries, the composition of the material was very uniform. This was attested by the very sharp γ′ solvus event detected using DSC. The hardness of CM247LC in this condition was significantly lower than that of CM247LC in the SLM+HT and conventionally cast states. This can be attributed to the very fine γ′ precipitates present in the microstructure in the as-SLM state, which were of the order of 5 nm. This size is well below the transition from weak to strong dislocation coupling expected in superalloys [31,32] and therefore the precipitates offer very limited resistance to dislocation motion. Much of the strength of the alloy was restored by post deposition heat treatment, which led to localised recovery and recrystallisation in the microstructure. With the heat treatment conditions used in this study, the extent of recrystallisation was limited and, as such, a strong cube texture was preserved. These changes were accompanied by coarsening of the γ′ precipitates to a scale comparable to that of the conventionally cast microstructure. Notably, the morphology of the MC carbides was unaffected by the heat treatment and were similar to that of the conventionally cast material. Although, data acquired using X-ray diffraction, **Fig. 14**,

indicated that the composition of the MC carbides changed following heat treatment. This in turn suggests that metastable MC carbides were produced as a result of the rapid cooling during SLM processing and that solute may have been exchanged with the matrix to form more stable carbides during heat treatment.

Two types of defects were observed in the SLM material, porosity and cracking. The porosity was attributed to gas released from the molten material, whilst the crack occurred as a result of the high thermal stresses generated during deposition and cooling. In principle, both defects may be controlled by process optimisation and cleanliness. In the material examined in this study, the cracks were the more prevalent and concerning defect. A previous study by Carter *et al.* [16] on selective laser melted CM247LC suggested ductility dip cracking as the cracking mechanism. This cracking mechanism is known to occur during welding of nickel-based superalloys [33,34]. However, the observations made in this study were not consistent with the ductility dip cracking. Critically, cracks follow grain and cell boundaries, which have been shown to have high dislocations densities. This suggests that the cracking is intimately linked with thermal contraction stresses of the cellular networks. The application of the post-SLM heat-treatment did partially alleviate the stresses present in the microstructure, as evidenced by the diminution of the dislocation content through recovery and recrystallisation. However, the heat treatment selected for this study led to the localised occurrences of both of these processes within the microstructure. For practical application of components fabricated using SLM processing it may be preferable to have an exclusively recovered or recrystallised microstructure. Alternative heat-treatments should therefore be selected at different temperatures that favour one or other of these processes. Critically, such heat treatments are not able to eliminate cracks formed during SLM. As such, post-fabrication HIPing may be required and, indeed, previous studies have shown promising results from HIPed material [16].

5. Conclusions

In this study, detailed characterisation of the microstructure of the nickel-base superalloy CM247LC has been performed following SLM processing and after subsequent heat treatment. SEM-EBSD characterisation revealed the presence of an elongated cellular microstructure with a strong cube texture in the build direction. The cells were observed

18

to be misorientated with respect to one another, leading to progressive variations in misorientation across cell colonies. Higher resolution imaging using TEM identified the presence of about 5 nm sized intracellular γ′ precipitates, about 50 nm inter-cellular γ′ precipitates and numerous dislocations located at the grain and cell boundaries. Following post-SLM heat treatment, partial recovery and recystallisation of the microstructure was observed. Recovery reduced dislocation densities between cells and allowed agglomeration of well-orientated cells to form grains. The limited occurrences of recrystallisation observed generated randomly orientated grains with no internal misorientations. Following heat treatment, coarsening of the γ′ precipitates to a size similar to that seen in conventionally cast and heat treated CM247LC was also seen, accompanied by an increase in hardness to a level more comparable to conventionally cast material. Gas-induced porosity was observed in the microstructure following the SLM process along with cracking, particularly near the periphery of the samples. The cracking followed cellular boundaries. This was consistent with the high density of dislocations imaged in these regions as well as stress concentrations arising as a result of local misorientations between adjacent cells.

References
[1] Sun Z, Ion JC. Laser welding of dissimilar metal combinations-Review. Journal of Materials Science 1995;30:4205-4214.
[2] Kruth JP, Leu MC, Nakagawa T. Progress in additive manufacturing and rapid prototyping, Annals of the CRIP 1998;47:525-540.
[3] Santos EC, Shiomi M, Osakada K, Laoui T. Rapid manufacturing of metal components by laser forming. International Journal of Machine Tools & Manufacture 2006;46:1459-1468.
[4] Gu DD, Meiners W, Wissenbach K, Poprawe R. Laser additive manufacturing of metallic components: materials, processes and mechanisms. International Materials Reviews 2012; 57:133-164.
[5] Clark D, Bache MR, Whittaker MT. Shaped metal deposition of a nickel alloy for aero engine applications. Journal of Materials Processing Technology 2008;203:439-448.
[6] Gaumann M, Bezencon C, Canalis P, Kurz W. Single-crystal laser deposition of superalloys: Processing-microstructure maps. Acta Materialia 2001;49:1051-1062.
[7] Dinda GP, Dasgupta AK, Mazumder J. Laser aided direct metal deposition of Inconel 625

superalloy: Microstructural evolution and thermal stability. Materials Science and Engineering A 2009;509:98-104.

[8] Chen J, Xue L, Wang SH. Experimental studies on process-induced morphological characteristics of macro- and microstructures in laser consolidated alloys. Journal of Materials Science 2011;46:5859-5875.

[9] Rosenthal R, West DRF. Continuous γ' precipitation in directionally solidified IN738LC alloy. Materials Science and Technology 1999;15:1387-1394.

[10] Mitchell A, Wang T. Solidification and precipitation in IN718. Superalloys 718, 625, 706 and Various Derivatives 2001:81-90.

[11] Parimi LL, Ravi GA, Clark D, Attallah MM. Microstructural and texture development in direct laser fabricated IN718. Materials Characterization 2014;89:102-111.

[12] Dinda GP, Dasgupta AK, Mazumder J. Texture control during laser deposition of nickel-based superalloy. Scripta Materialia 2012;67:503-506.

[13] Carter LN, Martin C, Withers PJ, Attallah MM. The influence of the laser scan strategy on grain structure and cracking behaviour in SLM powder-bed fabricated nickel superalloy. Journal of Alloys and Compounds 2014;15:338-347.

[14] Wei HL, Mazumder J, Debroy T. Evolution of solidification texture during additive manufacturing. Scientific Reports 5, 16446; doi: 10.1038/srep16446 (2015).

[15] Kanagarajah P, Brenne F, Niendorf T, Maier HJ. Inconel 939 processed by selective laser melting: Effect of microstructure and temperature on the mechanical properties under static and cyclic loading. Materials Science & Engineering A 2013;588:188-195.

[16] Kunze K, Etter T, Grässlin J, Shklover V. Texture anisotropy in microstructure and mechanical properties of IN738LC alloy processed by selective laser melting (SLM). Materials Science and Engineering A 2015;620:213-222.

[17] Zhang D, Niu W, Cao X, Liu Z. Effect of standard heat treatment on the microstructure and mechanical properties of selective laser melting manufactured Inconel 718 superalloy. Materials Science and Engineering: A 2015;644:32-40.

[18] Amato KN, Gaytan SM, Murr LE, Martinez E, Shindo PW, Hernandez J, Collins S, Medina F. Microstructure and mechanical behavior of Inconel 718 fabricated by selective laser melting. Acta Materialia 2012;60:2229-2239.

[19] Etter T, Kunze K, Geiger F, Meidani H. Reduction in mechanical anisotropy through high temperature heat treatment of Hastelloy X processed by Selective Laser Melting (SLM). IOP Conference Series: Materials Science and Engineering 2015;82:012097.

[20] Dimter M, Mayer R, Hummeler L, Salzberger R, Kotila J, Syvanen T. Method and device for manufacturing a three-dimensional object. US patent. No. US8034279B2; 2011.

[21] Hielscher R, Schaeben H, Siemes H, Orientation distribution within a single hematite crystal. Mathematical Geosciences 2010;42:359-375.

[22] ThermoCalc software, TCS Ni-based superalloy database, version 5, www.thermocalc.com; 2010.

[23] ThermoTech, ThermoTech Ni-based superalloys database version 8, www.thermocalc.com; 2011.

[24] Rasband WS. ImageJ, U.S. National Institute of Health, Besthesda, Maryland, USA, http://imagej.nih.gov/ij/, 1997-2015.

[25] Boettinger WJ, Kattner UR, Moon KW, Perepezko JH. DTA and heat-flux DSC measurements of alloy melting and freezing. National Institute of Standards and Technology Special publication 2006;960-15.

[26] Tan JC, Tan MJ. Dynamic continuous recrystallisation characteristics in two stage deformation of Mg-3Al-1Zn alloy sheet. Materials science and Engineering A 2003;339:124-132.

[27] Humphreys FJ, Hatherly M. Recrystallisation and related annealing phenomena. First edi., Pergamon, 1995.

[28] Huang HE, Koo CH. Effect of solution-treatment on microstructure and mechanical properties of cast fine-grain CM247LC superalloy. Materials Transactions 2004;45:1360-1366.

[29] Dubrovskaya LB, Zaytsev GB, Ordan'yan SS. Magnetic susceptibility of solid solutions of hafnium and tanatalum monocarbides, Fizika Metallov i Metallovedenie 1997;44:1316-1319.

[30] Norton JT, Mowry AL. Solubility relationships of the refractory monocarbides. Transactions of the American Institute of Mining, Metallurgical and Petroleum Engineers 1949;185:133-136.

[31] Jackson MP, Reed RC. Heat treatment of UDIMET 720Li- the effect of microstructure on properties, Materials science and Engineering A 1999;259:85-97.

[32] Collins DM, Stone HJ. A modeling approach to yield strength optimisation in a nickel-base superalloy. International Journal of Plasticity 2014;54:96-112.

[33] Ramirez AJ, Lippold JC. High temperature behaviour of Ni-base weld metal Part I. Ductility and microstructural characterisation. Materials science and Engineering A 2004;380:259-271.

[34] Ramirez AJ, Lippold JC. High temperature behaviour of Ni-base weld metal Part II. Insight into the mechanism for ductility dip cracking. Materials science and Engineering A 2004;380:245-258.

Table

Tab. 1: Nominal composition (wt.%) of CM247LC pre-alloyed powder used for SLM.

Tab. 2: Phase transition temperatures (˚C) obtained from the DSC thermograms on heating, as well as the values predicted using Thermocalc with the TCNI5 and TCNI8 databases.

Figure

Fig. 1: Micrograph showing the distribution and morphology of powder particles used for SLM process.

Fig. 2: Schematic representation of the laser deposition strategy used showing: (a) layer consolidation along the build direction (Z); (b) overview of three successive layers along the Z direction with a 67˚ rotation between them, (c) stripe design adopted within each layer and, (d) back and forth laser scan pattern used for consolidating each stripe.

Fig. 3: DSC thermograms on heating CM247LC in the as-SLM, SLM+HT and CC states. T_S is the solidus temperature, T_C is the carbide dissolution temperature, T_L is the liquidus temperature and $\Delta T_{\gamma'}$ is the γ' dissolution temperature range.

Fig. 4: Fraction of different phases as a function of temperature in CM247LC predicted using ThermoCalc with the TCNI5 and TCNI8 databases.

Fig. 5: BSE SEM micrographs of as-SLM CM247LC sectioned along (a) the longitudinal direction and (b) the transverse direction. EBSD IPF-Z maps corresponding to (a) and (b) are shown in (c) and (d), respectively. Equivalent IGM maps are shown in (e) and (f).

Fig. 6: {001} pole figures obtained from the EBSD data acquired from the (a) longitudinal and, (b) transverse sections of as-SLM CM247LC shown in Fig. 5c and d, along with normalised histograms of the inter-granular misorientation distributions weighted by the grain area from the (c) longitudinal and (d) transverse sections.

Fig. 7: (a) BSE SEM micrograph of a transverse section of as-SLM CM247LC showing a grain composed of multiple cells and, (b) corresponding misorientation map centered around the mean orientation of the grain (red cross in the IPF-Z and colour map). The blue points in the IPF-Z and colour map indicate the orientations of the individual data points. For clarity, only 5% of all of the available data points have been included in the colour map.

Fig. 8: (a) Selected area bright field TEM image of a transverse section of the as-SLM specimen showing the cell structure and, (b) corresponding [110] selected area diffraction pattern. Faint superlattice reflections originated from the γ' precipitates are also indexed. (c) Selected area bright field TEM image of a transverse section of the as-SLM specimen showing the band structure of cells.

Fig.9: TEM dark field images generated from a γ' superlattice reflection: (a) Image showing a bimodal distribution of γ' precipitates; (b) Higher magnification image showing intra-cellular γ' precipitates, identified by the presence of Moiré fringes.

Fig.10: TEM HAADF image of several cells of CM247LC in the as-SLM condition along with STEM-EDX area maps of the principal alloying elements. The electron transition from which the concentration of each element was determined is identified in the figure.

Fig. 11: BSE SEM micrographs of SLM+HT CM247LC sectioned along (a) the longitudinal direction and, (b) the transverse direction. EBSD IPF-Z maps corresponding to (a) and (b) are shown in (c) and (d), respectively. Equivalent IGM maps are shown in (e) and (f).

Fig.12: {001} pole figures obtained from the EBSD data acquired from the (a) longitudinal and (b) transverse sections of SLM+HT CM247LC shown in Fig.11c & d, along with normalised histograms of the inter-granular misorientation distributions weighted by the grain area from the (c) longitudinal and (d) transverse sections.

Fig.13: (a) BSE SEM micrograph of the SLM+HT specimen showing the bimodal distribution of γ'. (b) TEM bright field image of an unrecrystallised region of the sample. (c) TEM dark field image generated from a γ' superlattice reflection of a recrystallised region.

Fig.14: XRD spectra of CM247LC in the as-SLM, SLM+HT and CC states.

Fig.15: BSE SEM micrographs of: (a) A transverse section near the periphery of an as-SLM CM247LC sample showing the presence of cracks; (b) Higher magnification image showing preferential propagation of the crack along the cell boundaries.

Fig.16: BSE SEM micrographs of conventionally cast CM247LC in the solution heat treated condition displaying; (a) grain structure and carbides, and, (b) higher magnification image showing the secondary and tertiary γ' precipitates.
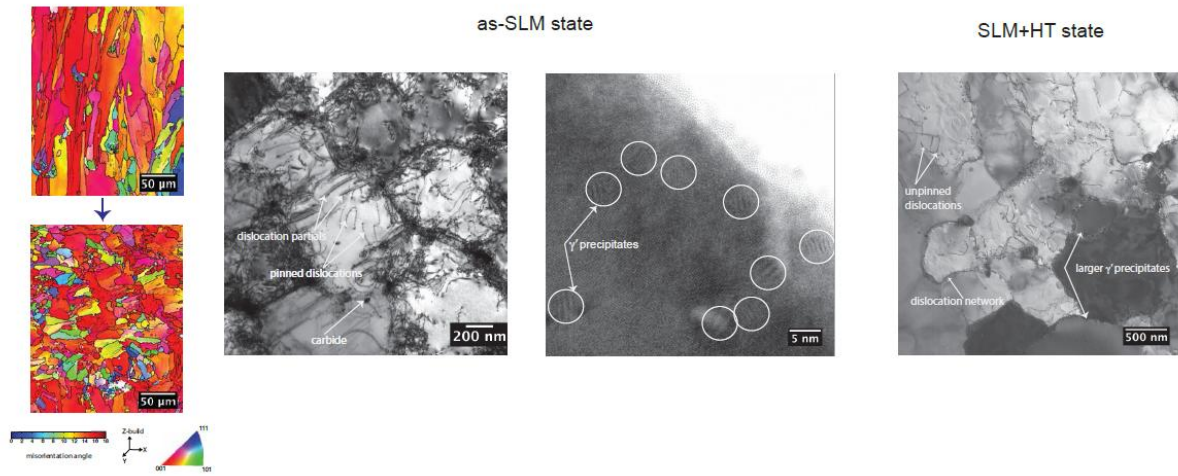
Table 1

	Ni	Cr	Co	Mo	W	Ta	Al	Ti	Hf	C	B	Zr
	61.51	8.11	9.41	0.52	9.66	3.18	5.49	0.74	1.29	0.08	0.013	0.008

Table 2

Phase transformation	DSC measurements			ThermoCalc-predictions	
	as-SLM	SLM+HT	CC	TCNI5	TTNI8
$\Delta T\gamma' = T_{\gamma'\,start} - T_{\gamma'\,end}$	1254-1265	1246-1265	1239-1252	1257	1209
Solidus, T_s	1279	1279	1295	1257	1297
Carbide dissolution, T_c	1357	1356	1355	1293	1358
Liquidus, T_L	1373	1373	1373	1385	1372

Graphical abstract